PAPER

Highly efficient WO₃–ZnO mixed oxides for photocatalysis

Sangeeta Adhikari,[a] Debasish Sarkar*[a] and Giridhar Madras[b]

Monoclinic nanocuboid WO_3 enhanced the photocatalyst efficiency of quasi nanobelt zinc oxide for dye degradation in the presence of visible light radiation. Combustion synthesized ZnO resulted in a belt-like morphology through *in situ* cluster formation of near spherical particles but homogenously disperses and strongly adheres to nanocuboid WO_3 during physical mixing. Cationic methylene blue (MB) and anionic orange G (OG) undergo degradation through a charge transfer mechanism in the presence of WO_3–ZnO (1 : 9 weight percentage ratio) mixture. The photocatalytic reaction was enhanced due to the reduction in the recombination of photogenerated electron–holes. The high degree of 90% degradation of both dyes is due to the activity of the mixed oxides, which is much higher than that obtained either with WO_3 or ZnO individually.

1. Introduction

Semiconductors have been extensively studied to degrade organic pollutants in water.[1] The pollutants can be removed using physicochemical methods like adsorption,[2] membrane separations,[3] nanofiltration,[4] biosorption,[5] electrochemical methods,[6] *etc.* However, this is only a transfer of pollutants from one system to another. In this perspective, the advanced oxidation process (AOP) has been suggested as a good technique for the degradation of pollutants and decolorizing contaminated water.[7,8] Semiconducting materials like MnO_2, TiO_2–polyaniline composite and WS_2/WO_3 nanoparticles are well studied for photocurrent response under UV light.[9–11] Among them, titanium dioxide (TiO_2) is the most studied photocatalyst due to its high photochemical efficiency, stability, low cost and non-toxic nature. A suitable alternative to this particular material is ZnO as it possesses similar band gap and absorbs in the solar spectrum in larger fraction than TiO_2.[12] However, the photogenerated charge carrier undergoes rapid recombination and lowers the photocatalyst efficiency. Since the generation of charge carriers is one of the key factors for the degradation of organic pollutants, their recombination is detrimental to achieve high photocatalytic efficiency. To solve this problem, recombination of the photogenerated charge carriers has to be suppressed with necessary modification to the material.

Zinc oxide with band gap of 3.2 eV is capable of absorbing irradiation in UV wavelength, but UV is only 4% of total solar light.[13] Thus, the prime objective remains in surface modification of a semiconductor photocatalyst to achieve higher light absorption capacity by shifting the absorbance to the visible wavelength.[14,15] Hence, an attempt has been made to restrict the e^-–h^+ recombination phenomenon of ZnO and increase the photocatalytic efficiency by mixing of low band gap semiconductors.[16] Low band gap semiconductor WO_3 has emerging potential for electrochromic behavior in presence of visible wavelength, which can be mixed with ZnO for photocatalytic degradation.[17–19] Hence, different combinations of morphology and crystal structure for both WO_3 and ZnO should be optimized to achieve maximum photocatalytic efficiency.[20–23]

Several synthetic methods have been attempted to fulfil this requirement, but evaluation of their cumulative efficiency of these mixed oxides is limited in recent literature.[24,25] WO_3–ZnO mixed oxide is prepared in one step and 17.2% degradation efficiency has been achieved for methyl orange in the presence of 5 mol% WO_3 under light irradiation.[26] In addition, commercial grade ZnO has been used to prepare modified WO_3–ZnO rod mixed oxide through hydrothermal method and reported 44% photocatalytic efficiency for 5 at% WO_3.[24] Co-precipitation followed by calcination resulted in a WO_3–ZnO composite, which showed 53% degradation efficiency of acid orange II in the presence of 8 wt% WO_3.[25]

In this study, we have determined the optimum amount of WO_3 with ZnO that exhibits the maximum photodegradation efficiency for the degradation of both the cationic and anionic dyes. For this purpose, WO_3 nanocuboids and ZnO rectangular slabs were synthesized by the hydrothermal and combustion method, respectively. The details of the phase, crystal structure, morphology and surface area of WO_3, ZnO and WO_3–ZnO mixed oxide composites has been studied systematically. Furthermore, band gap and photoluminescence measurement has been performed to understand the photocatalytic activity of

[a]Department of Ceramic Engineering, National Institute of Technology, Rourkela, India. E-mail: dsarkar@nitrkl.ac.in; Tel: +91-0661-2462207

[b]Department of Chemical Engineering, Indian Institute of Science, Bangalore, India

optimum WO_3 loaded ZnO for the degradation of both dyes under visible light irradiation.

2. Experimental procedure

2.1. Synthesis of WO_3 nanocuboids

Analytical grade chemicals were used without further purification. WO_3 nanocuboid was hydrothermally synthesized using fluoroboric acid (HBF_4) as structure directing agent. A precipitate was formed while addition of 4 M HBF_4 and $Na_2WO_4 \cdot 2H_2O$. The above solution was hydrothermally treated at 180 °C for 6 h to yield WO_3 nanocuboids. The detailed process optimization has been mentioned elsewhere.[17]

2.2. Synthesis of ZnO nanoparticles

Zinc oxide (ZnO) nanoparticles were synthesized by wet-chemical combustion method. In a typical synthesis, stoichiometric quantities of zinc nitrate hexahydrate and oxalic acid was taken in crystallization dish (50 × 100 mm) and dissolved in minimum amount of water at room temperature to form clear solution. The prepared aqueous solution was kept in a pre-heated muffle furnace at 450 ± 10 °C until complete combustion. Initially, the furnace was opened to allow passage of sufficient air for the completion of chemical reaction and formation of white porous mass. Herein, the described ZnO quasi fiber process optimization is described in details somewhere else.[27] The obtained dry, porous material was ground using mortar and pestle, and used for preparation of WO_3–ZnO mixed oxides.

2.3. Preparation of mixed oxides

For the preparation of WO_3–ZnO mixed oxides, known amounts of WO_3 & ZnO nanopowders with different weight ratios (0, 10, 20, 30, 40, 50 and 100) was ground well for about 30 min. The mixture was then suspended in 20 ml water followed by ultrasonication for 1 h to form a colloidal solution. The solution was oven dried at 80 °C and subsequently heat treated at 450 °C for 2 h in oxygen to ensure the effective mixing of photoactive mixed oxide catalyst. The catalysts were characterized through XRD, TEM, UV-DRS and photoluminescence measurements. This mixture was used for photocatalytic experiments without any further modification.

2.4. Irradiation assessment

The photocatalytic experiment was carried in a setup consisting of jacketed quartz tube with jacketed Pyrex slurry reactor enclosed in a rectangular hard wood casing. A 400 W metal halide lamp (Philips-India, λ_{max} = 510 nm) was placed in the quartz tube. The set of quartz tube and lamp was gently placed inside a slurry reactor. Water supply was provided through jacket of quartz tube and slurry reactor to avoid thermal degradation, and temperature at 29 ± 2 °C. The dye solution was kept in a slurry reactor and lamp was positioned 2 cm above from the top level of the suspension. In the present system, photocatalytic performance of both cationic, methylene blue (MB) and anionic orange G (OG) dye was performed in the

presence of mixed oxide catalyst. 50 mg of the catalyst was dispersed in 10 ppm concentrated 50 ml aqueous solution of dye. The dye solution along with the catalyst was kept in a dark environment with stirring for 2 h to establish adsorption/desorption equilibrium. The aliquot ∼5 ml containing dye and powder catalyst was taken out at given time intervals and was centrifuged at 3000 rpm for 10 min. After the catalyst separation, the change in dye concentration was determined through change in absorbance with a UV-vis spectrophotometer. The absorbance value of methylene blue and orange G was taken at 664 nm and 476 nm, respectively. After each measurement, the aliquot along with the catalyst was transferred back to the reaction slurry to avoid volume and concentration change of both the dye and catalyst. The catalytic experiments were repeated thrice and the relative error was less than ±3%. The optimized catalyst was compared with the standard photocatalyst Degussa P25 TiO_2.

2.5. Analytical methods

X-ray diffraction (XRD) patterns for the powders were obtained using a Philips X-ray diffractometer with Ni filtered Cu-Kα radiation (λ = 1.5418 Å). FESEM images for individual WO_3 nanocuboids, ZnO rectangular slabs and optimized mixed oxide was carried out using NOVA NANOSEM FEI-450 system. The powder was mounted on a double-sided carbon tape attached to a SEM stub and sputter coated with gold for 2 min. Specific surface area of optimized powder was measured using nitrogen as the adsorbate in a BET apparatus (QuantachromeAutosorb, USA). Morphology was studied by transmission electron microscope (JEOL JEM-2100). UV-DRS measurement was done through Shimadzu spectrophotometer (UV-2450) to evaluate the band gap energy of WO_3, ZnO and WO_3–ZnO mixed oxides in the wavelength region of 200–800 nm. Photoluminescence spectrum was measured using Hitachi F-4500 spectrofluorimeter. The excitation was made at 350 nm.

3. Results and discussions

3.1. Phase analysis of WO_3–ZnO mixed oxides

XRD patterns of synthesized WO_3, ZnO and WO_3–ZnO mixed oxide composites are represented in Fig. 1. The characteristic indexed diffraction patterns of WO_3 and ZnO corresponds to the monoclinic crystal phase (Fig. 1a) and hexagonal wurtzite phase (Fig. 1b), respectively. No impurity peaks were observed for both the powders. The obtained diffraction peaks of WO_3 and ZnO matches well with the JCPDS file no. 72-0677 (space group $P21/n$, a = 7.3 Å, b = 7.54 Å, c = 7.69 Å, $\alpha = \gamma$ = 90.00° and β = 90.88°) and JCPDS file no. 75-0576 (space group $P63mc$, $a = b$ = 3.24 Å, c = 5.19 Å, $\alpha = \beta$ = 90.00° and γ = 120°), respectively. Fig. 1c represents the XRD pattern of the prepared WO_3–ZnO mixed oxide catalysts. Constant and clear distinct peak intensity indicates the different percentage content of individual WO_3 and ZnO, respectively. The result depicts the physical content homogenization in the mixture that is further confirmed through SEM elemental mapping in the later section.
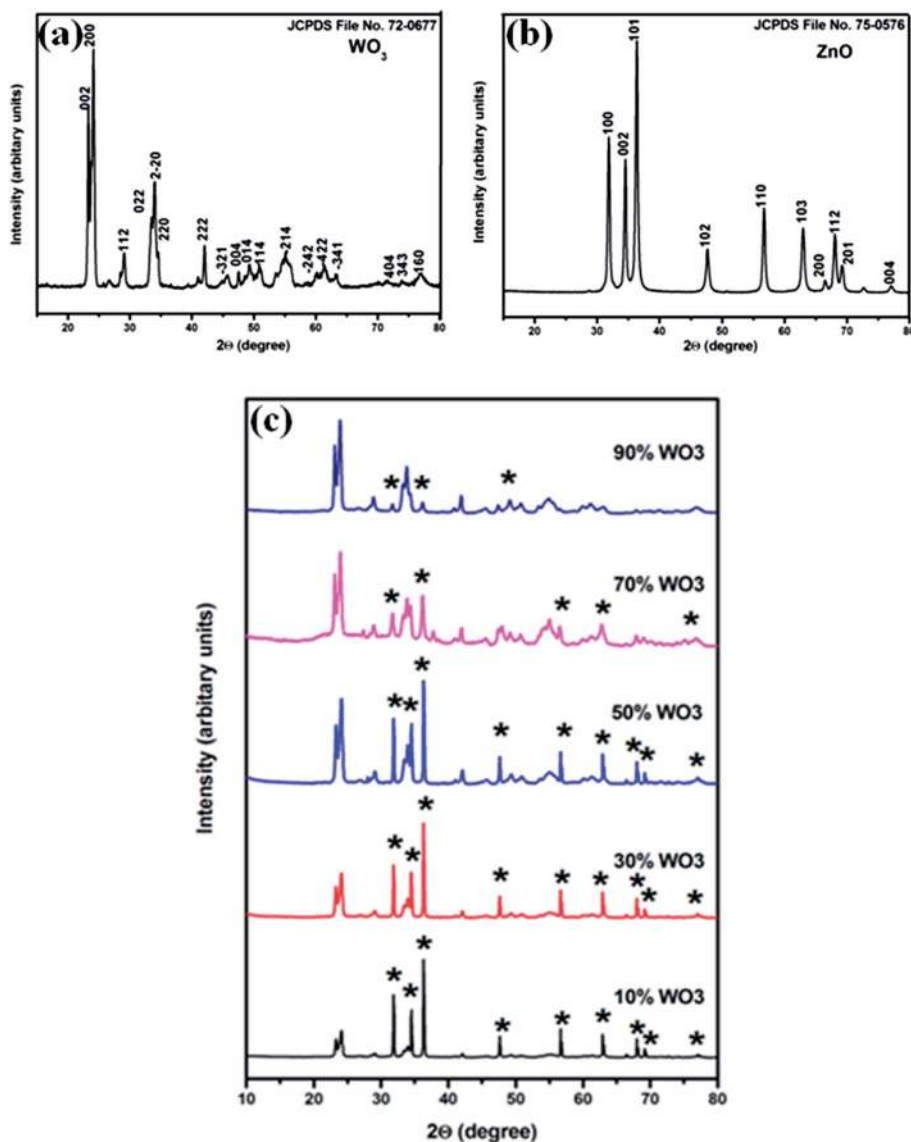
Fig. 1 XRD patterns of (a) WO_3, (b) ZnO and (c) composite pattern of WO_3–ZnO mixed oxides (* represents the ZnO in the composites).

3.2. Morphological analysis of oxides

Field-emission scanning electron microscopic analysis including elemental distribution depicts the particle morphology and distribution phenomenon as illustrated in Fig. 2. Fig. 2a shows the soft agglomerated WO_3 nanoparticles, where high magnification reveals the cuboid morphology with average dimensions of 140/115/85 nm^3. Bunched fiber ZnO particles are visualized after combustion synthesis in Fig. 2b. The average particle size of the ZnO rod is found to be of length ∼3 μm and breadth ∼0.8 μm, respectively. However, this bundled ZnO is a cluster of near spherical particles that has agglomerated during the rapid combustion process. A representative FESEM and elemental mapping of an optimum 10% WO_3–ZnO mixed oxide catalyst is shown in Fig. 2c and d, respectively. The uniform distribution of elements W, Zn and O predicts the intimate attachment within oxides, where ZnO appears as spherical nature of particles rather than rod shape.

Interactive mixing within two different particles is necessary for the effective photocatalytic efficiency, which is further confirmed by TEM analysis after dispersion in liquid media.

More precise particle morphology information is determined from TEM and SAED pattern of the samples, as shown in Fig. 3. A distinct cuboid morphology of soft agglomerated WO_3 nanoparticles has an average particle length of ∼152 nm and width ∼120 nm (Fig. 3a). The imperfect edge of each cuboid particle with blurred thickness is attributed to tilting of particles at certain angles. Selected area electron diffraction (SAED) pattern of WO_3 nanocuboid is shown in Fig. 3b. An ordered array of spot is observed because of the single crystalline nature of the particle. Fig. 3c shows ZnO rod shaped structure formed from hard agglomeration of spherical particles, as visualized from the image. Combustion is an exothermic process which promotes rapid formation of near spherical particles and their *in situ* welding of a particular direction to form a fibrous like
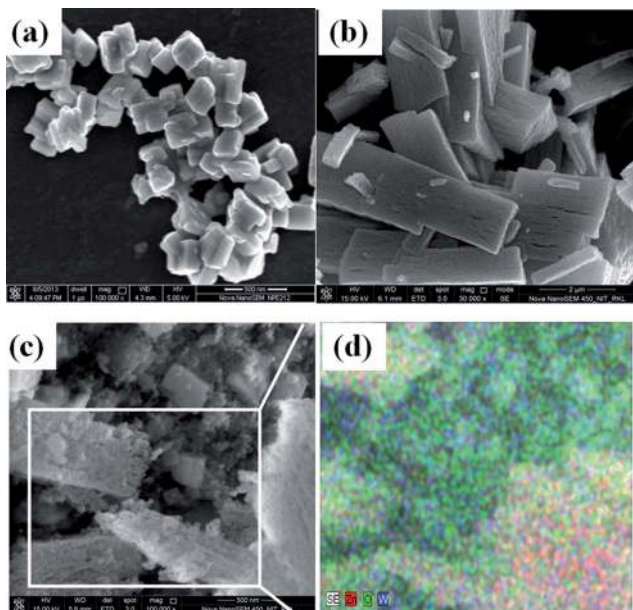
Fig. 2 FESEM images of (a) WO_3 (inset shows the high magnification image), (b) ZnO, (c) 10% WO_3/ZnO, (d) SEM/EDS elemental mapping of 10% WO_3/ZnO.

Fig. 3 TEM images of (a) WO_3, (c) ZnO, (e) 10% WO_3/ZnO and SAED patterns of (b) WO_3, (d) ZnO and (f) 10% WO_3/ZnO.

structure. A similar type 2D film of spinel ferrite instead of 1D quasi fiber formation during auto-combustion synthesis has been reported by Sutka et al.[28]

Herein, the average particle size of the primary sphere is found to be ~60 nm. The concentric circle in SAED pattern represents the crystalline nature of the soft agglomerated particles (Fig. 3d). Fig. 3e shows the mixture of WO_3 nanocuboid and spherical ZnO particles for an optimum composition of 10% WO_3–ZnO composite oxides. The particles are well embedded and attached to one another even after well dispersion through ultrasonication, as seen from the TEM image. This embedded system is a favourable accomplishment to achieve high degree of photochemical reaction, which is described later. The corresponding SAED pattern in Fig. 3f exhibits an ordered pattern from single crystal WO_3 nanocuboid and concentric circles from agglomerated ZnO spherical particles.

The specific BET surface area of WO_3 nanocuboid and ZnO spherical particles forming rod structure is found to be 5.16 $m^2 g^{-1}$ and 17.8 $m^2 g^{-1}$, respectively. The BET surface area of 10% WO_3–ZnO was found to be 15.9 $m^2 g^{-1}$. The specific BET surface areas of all the composites have been tabulated in Table 1. The surface area of different weight ratio WO_3–ZnO decreases with increasing WO_3 content.

3.3. UV-DRS and band gap calculation

The Kubelka–Munk (Fig. 4a) unit of absorption of WO_3, ZnO and WO_3–ZnO mixed oxide composites has been calculated from the following equation: $F(R) = (1 - R)^2/2R$ (where R is the reflectance).[29] It is observed that the absorption band is in the wavelength between 380 and 520 nm for all WO_3, ZnO and WO_3–ZnO mixed oxide composites. Broad tails are observed for WO_3–ZnO mixed oxide samples. The mixed oxide composite
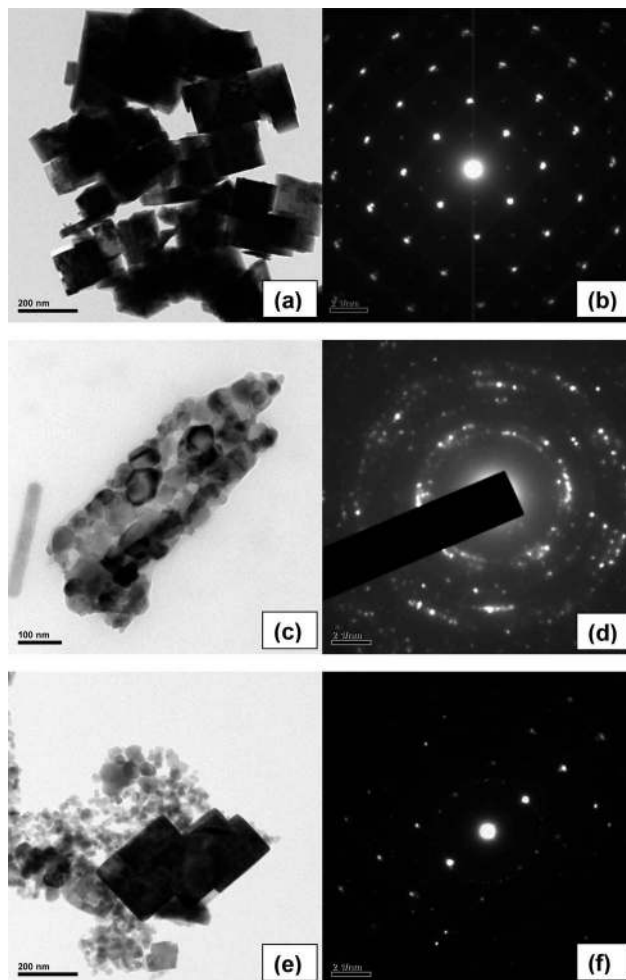
shows a slight red shift of band gap absorption in comparison to the pure ZnO. With addition of WO_3 to ZnO, there is the formation of the defect energy levels within the forbidden band that initially increases the band gap energy to 2.98 eV and then decreases with increased loading of the WO_3 in the mixed oxide composites. Band gap energy was estimated using Tauc plot and the extrapolation of the linear slope to photon energy, as shown in Fig. 4b. The calculated band gap energy

Table 1 Surface and adsorption properties of WO_3–ZnO mixed oxides

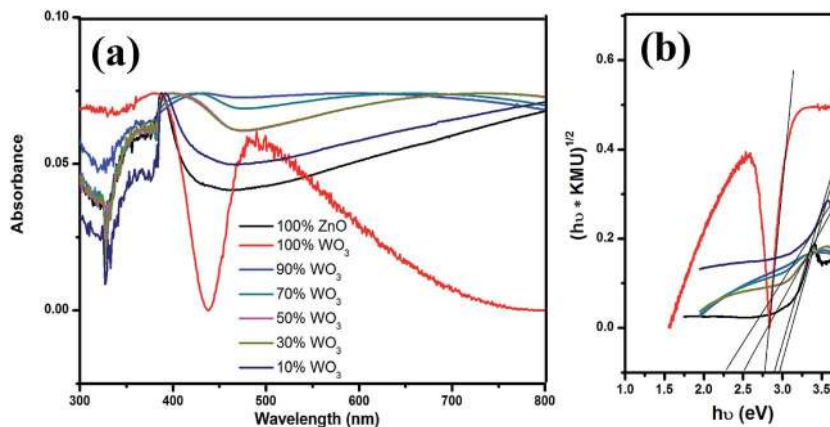| Catalyst	Surface area ($m^2 g^{-1}$)	Band gap (eV)	Methylene blue % Adsorption	Orange G % Adsorption
100% ZnO	17.8	2.95	8%	0%
10% WO_3	15.9	2.98	10%	0%
30% WO_3	14.5	2.52	10%	0%
50% WO_3	11.6	2.55	12%	0%
70% WO_3	9.4	2.25	13%	0%
90% WO_3	6.8	2.25	15%	0%
100% WO_3	5.16	2.78	17%	0%

Fig. 4 UV-vis absorbance spectra of WO$_3$, ZnO and WO$_3$–ZnO mixed oxide composites with different WO$_3$ loading.

has been tabulated in Table 1. The band gap of WO$_3$ and ZnO is found to be 2.78 eV and 2.95 eV, respectively. The energy band gap of 10% WO$_3$–ZnO mixed oxide composite is almost similar to ZnO that is 2.95 eV but the resultant band gap decreases to 2.25 eV with increasing WO$_3$ content. However, an optimum content is required to reduce the recombination effect of ZnO.

3.4. Photocatalytic measurements

During the photochemical reaction, adsorption of dye over the catalyst is an important phenomenon to understand the surface reactivity of the catalyst towards dye before photocatalysis. Thus, the dye solution along with the catalyst was kept in dark with rigorous stirring for 2 h to establish adsorption equilibrium. The adsorption of MB in the presence of different mixed oxide has been tabulated in Table 1. Maximum and minimum adsorption of 17% and 8% was observed for WO$_3$ and ZnO, respectively. OG does not show adsorption till 2 h in the presence of the catalysts. The concentration of the dyes after adsorption was taken as the initial concentration for degradation. The photolysis was carried to understand the photosensitization of dye. In the present experiments, methylene blue and orange G dye was irradiated for 2 h in the absence of any catalyst but in the presence of light and less than 7% degradation was observed in all cases.

The testing of photocatalytic activity for degradation of MB and OG solution has been carried under metal halide light irradiation. The degradation profile of the MB and OG dye solution with respect to different WO$_3$ loading (0, 10, 20, 30, 40, 50, and 100 wt%) has been represented in Fig. 5a and b, respectively. The zero time in Fig. 5 and 6 corresponds to 2 h after completion of adsorption equilibrium. Thus, the initial concentration for catalysis is the concentration at the end of the adsorption *i.e.*, after 2 h. The degradation profile of the mixed composites is given by C/C_o, where, C and C_o are the concentrations at different time intervals and at initial time, respectively. It is clearly evident from the degradation profile (Fig. 5a and b) that 10% of WO$_3$ loading in ZnO shows faster

decolourization for both MB and OG under visible light irradiation than ZnO and WO$_3$. Initially, WO$_3$ shows lower activity as compared to ZnO but with the decrement of WO$_3$ loading in ZnO, catalytic activity increases as evident from figure. The composite with 10% WO$_3$ in ZnO shows 30% higher activity
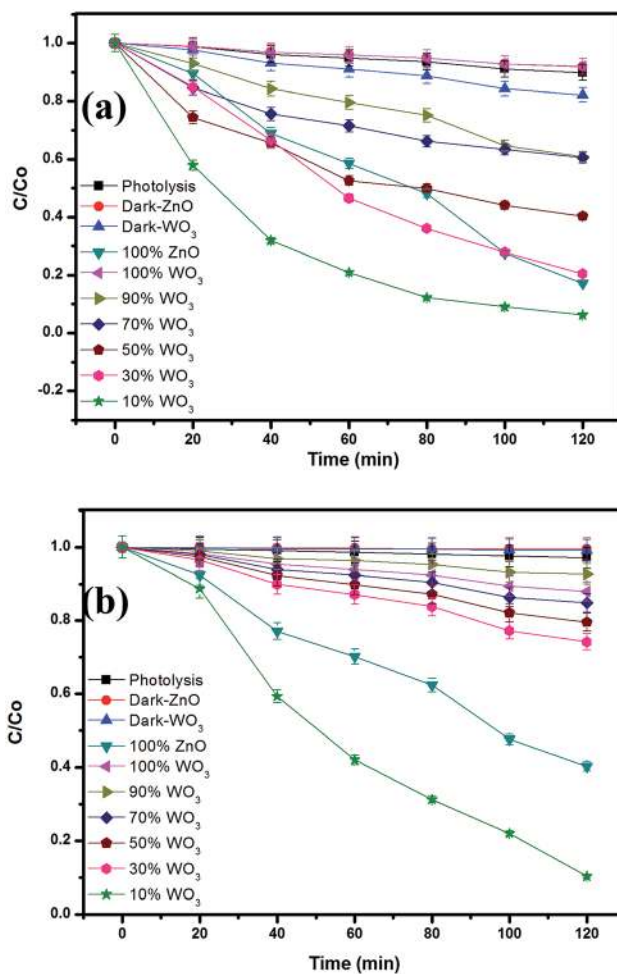

Fig. 5 Degradation profile of (a) MB and (b) OG with different mixed oxide composites.
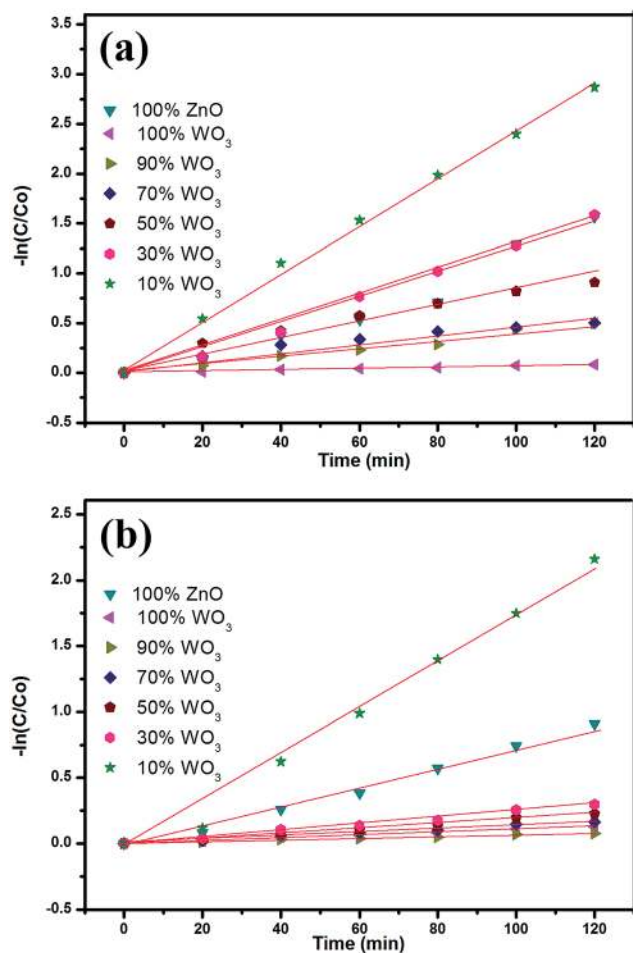
Fig. 6 Kinetic studies of (a) MB and (b) OG degradation with different mixed oxide composites.
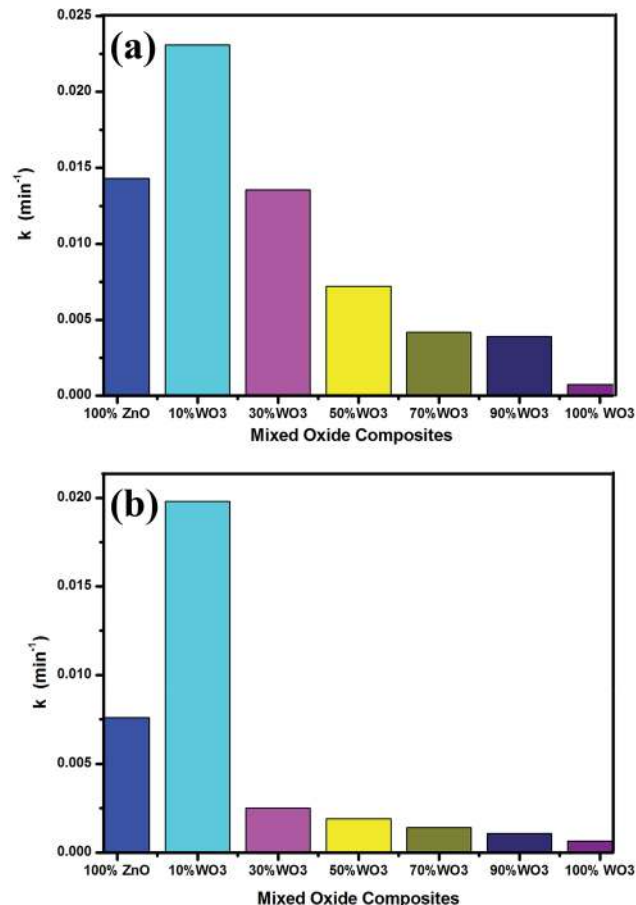

Fig. 7 Rate constant chart of (a) MB and (b) OG degradation with different mixed oxide composites.

than pure ZnO. High decolourization efficiency of 93% and 89% was observed for MB and OG, respectively.

The photocatalytic performance of the prepared WO_3–ZnO mixed oxide composite can be estimated from the kinetics of the photocatalytic degradation of the MB and OG dye solution, respectively. The photocatalytic degradation is governed by kinetics:[30,31] $-\ln(C/C_o) = kt$ where, C is the concentration at any time (t), C_o is the initial concentration, k is the apparent reaction rate constant and t is the reaction time. The kinetic rate constant can be obtained from the linear plot of $-\ln(C/C_o)$ with t. The slope obtained gives the rate constant k in min^{-1}. The kinetic plots for both MB and OG with different WO_3 loading is represented in Fig. 6a and b, respectively. The photodegradation for both the dyes is in accordance with the pseudo first-order kinetic reaction represented by the straight line fitting. The apparent reaction rate constant k (min^{-1}) for different mixed oxide composites for photodegradation of MB and OG has been calculated from the slope of the kinetic plot and shown in Fig. 7a and b, respectively. The obtained rate constant and correlation coefficient from plot is tabulated in Table 2. For comparison, the activity of Degussa P25 TiO_2 for both the dyes is also tested as control experiments under

identical conditions and presented in Fig. 8a and b. Approximately, 60% and 50% degradation is observed for MB and OG under visible light irradiation, which is less as compared to combustion synthesized ZnO and optimum WO_3–ZnO mixed oxide. This confirms that ZnO absorbs more energy in visible range than standard TiO_2 photocatalyst. It is observed that higher rate constant of 0.0231 min^{-1} and 0.0198 min^{-1} is found with 10% WO_3–ZnO mixed oxide composite for MB and OG, respectively. With decrease in WO_3 content in ZnO, the rate constant value increases thereby increasing the photocatalytic efficiency. The probable reason for increased activity could be attributed to the charge separation mechanism in the WO_3–ZnO mixed composites. The charge separation mechanism has been discussed in the later section. The electron–hole recombination probably reduces with an optimum WO_3 content. The reduction in recombination is further supported by the photoluminescence spectra of the mixed composites as discussed later. Although WO_3 has visible light absorption, lower activity is observed for its narrow band gap resulting in high recombination rate. Therefore, WO_3 can be coupled with other semiconductor materials for charge separation and better photochemical activity.

Table 2 Kinetic parameters of MB and OG degradation by WO$_3$–ZnO mixed oxides

Catalyst	Methylene blue			Orange G		
	% Degradation	$k \times 10^2$ (min^{-1})	R^2	% Degradation	$k \times 10^2$ (min^{-1})	R^2
100% ZnO	82	1.43	0.9822	59	0.76	0.9862
10% WO$_3$	93	2.31	0.9878	89	1.98	0.9837
30% WO$_3$	79	1.35	0.9930	25	0.25	0.9864
50% WO$_3$	59	0.72	0.9767	20	0.19	0.9886
70% WO$_3$	39	0.39	0.9797	15	0.14	0.9849
90% WO$_3$	39	0.41	0.9835	12	0.10	0.9906
100% WO$_3$	8	0.07	0.9905	7	0.06	0.9877
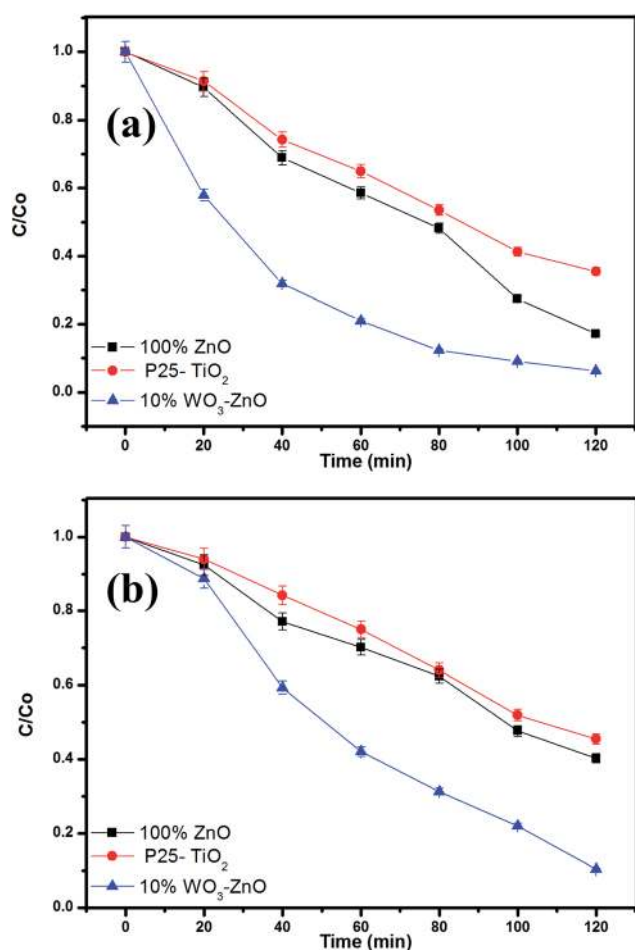
Fig. 8 (a) MB and (b) OG degradation profile in comparison with Degussa P25 TiO$_2$.

3.5. Reuse of the photocatalyst

Multiple use assessment predicts the long term performance and economic viability of photocatalyst. The reusability of the optimum 10 wt% WO$_3$ mixed ZnO describes the consecutive photocatalytic degradation efficiency for both MB and OG as shown in Fig. 9. Each time centrifugation of the catalyst was carried to remove the solid catalyst and the catalyst was dried at 100 °C for further use. Initially, 93% MB degradation is found in

1st run which decreases as 92%, 90% and 84% in 2nd, 3rd and 4th run, respectively (Fig. 9a). Similarly, OG degrades as 89%, 88%, 86% and 83% in 1st, 2nd, 3rd and 4th run, respectively (Fig. 9b). The photocatalytic activity decreases till 10% and 6% for MB and OG, respectively for 4 consecutive cycles, as observed from the figure. Each reusable experiment is carried after proper adsorption–desorption equilibrium. To better understand the material stabilization of the reused catalyst composite XRD pattern of the optimized catalyst and reused catalyst after 4th run is shown in Fig. 9c. XRD pattern shows no significant change in the crystal structure after four consecutive cyclic runs of the catalyst. One of the probable reasons for decreasing activity could be leaching of the surface during the photocatalytic reaction attributing to the loss of active support sites. Moreover, the consecutive heat treatment after each cycle decreases the surface area of the catalyst resulting in partial aggregation of catalyst. The organic intermediates that are formed during the catalytic process can also adsorb on the surface, thereby reducing the overall efficiency of the photocatalyst. In addition, loss of catalyst also occurs during repetitive runs resulting in reduced photoreactivity.[32] The above results suggest that the reactivity of the catalyst is completely effective till four consecutive cycles under metal halide irradiation. The working mechanism of the photocatalyst has been discussed in the later section.

3.6. Mechanism of mixed semiconductor photocatalyst

WO$_3$ and ZnO nanoparticles are typical semiconductors. Fig. 10 shows the possible energy storage mechanism of ZnO in presence of WO$_3$ when both are irradiated under visible light. The higher photocatalytic activity of the 10% WO$_3$–ZnO composite attributes to the energy level difference of WO$_3$ and ZnO that narrows the band gap. In the present system, WO$_3$ acts as absorber due to its absorption in visible region but narrow band gap (2.7 eV) facilitates the recombination of electron–hole pair through coupling with ZnO. When WO$_3$–ZnO mixed oxide composite is radiated by visible light, the activation of ZnO to produce the photogenerated electron–hole pairs is not possible due to its large absorption gap, while narrow band gap WO$_3$ can efficiently absorb the visible light and gets excited to generate electron–hole pairs. The photogenerated electrons generated in WO$_3$ transfer its electrons to
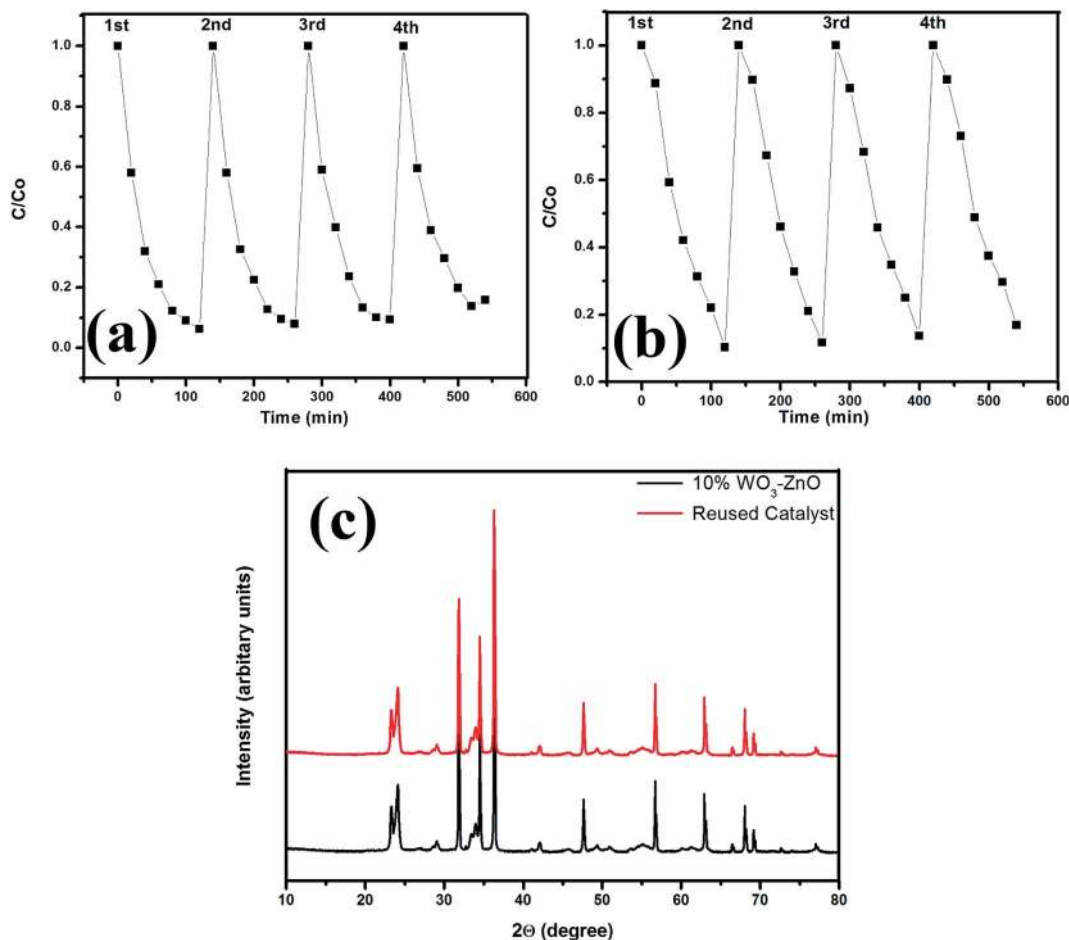
Fig. 9 Degradation profile on reusability of the 10% WO_3–ZnO mixed oxides (a) MB, (b) OG and (c) composite XRD pattern of the catalyst and after reuse.
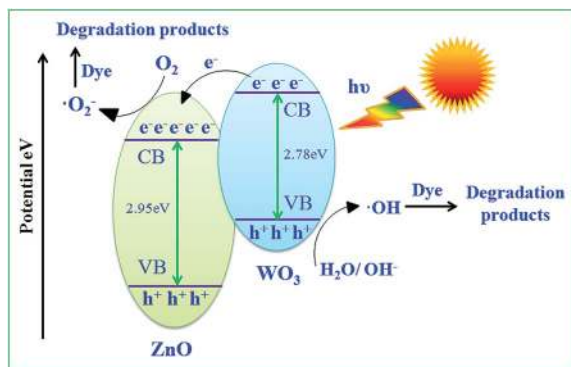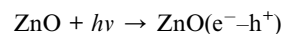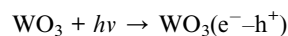

Fig. 10 Schematic mechanism of degradation by WO_3–ZnO mixed oxides.
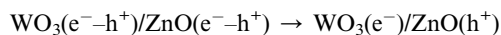
conduction band of ZnO reducing the probability of recombination of photogenerated electron–hole pairs and increasing the number of active species for degradation. Thus, ZnO plays the role of co-catalyst that traps the electron from further recombination. The photoelectrons easily traps the dissolved O_2 to form superoxide ($^\bullet O_2^-$) anion radical and photoinduced

holes trap OH^- to form $^\bullet OH$ radical to photodegrade dyes.[16,33] The reactivity of formed radicals $^\bullet OH$ and $^\bullet O_2^-$ are sufficient to efficiently degrade the organic dye molecules. The charge separation and probable photocatalytic reaction follows the steps given below:[34–36]
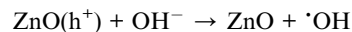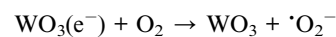
Electron–hole pair generation:

$$WO_3 + h\nu \rightarrow WO_3(e^- – h^+)$$

$$ZnO + h\nu \rightarrow ZnO(e^- – h^+)$$

Charge transfer reaction:

$$WO_3(e^- – h^+)/ZnO(e^- – h^+) \rightarrow WO_3(e^-)/ZnO(h^+)$$

Radical formation:

$$WO_3(e^-) + O_2 \rightarrow WO_3 + ^\bullet O_2^-$$

$$ZnO(h^+) + OH^- \rightarrow ZnO + ^\bullet OH$$

Dye degradation:

$$Dye + {}^\cdot O_2{}^- / {}^\cdot OH \rightarrow Mineral\ acids + CO_2\uparrow + H_2O$$

$$Dye + {}^\cdot OH \rightarrow Mineral\ acids + CO_2\uparrow + H_2O$$
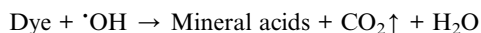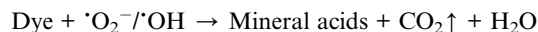
In order to determine the reactive radical species that are responsible for efficient photocatalysis, the dye solution was reacted in the presence of scavengers. Four different scavengers namely EDTA-2Na$^+$ (hole scavenger), tertiary-butyl alcohol (TBA, $^\cdot OH$ scavenger), dimethyl sulfoxide (DMSO, e$^-$ scavenger), benzoquinone (BQ, $O_2{}^{\cdot -}$ scavenger) were added to the dye solution and the degradation of the dye was monitored. It was observed that the presence of TBA and BQ significantly reduced the degradation. This indicates that $^\cdot OH$ and $^\cdot O_2{}^-$ generated during the reaction is primarily responsible for the degradation of the dyes under visible light radiation in the presence of the WO$_3$–TiO$_2$ mixture.

3.7. Photoluminescence study

The photo-recombination rate of electron–hole pair can be studied from the photoluminescence (PL) spectrum. Fig. 11 represents the composite PL spectrum of ZnO, WO$_3$, 70% WO$_3$, 50% WO$_3$ and 10% WO$_3$, respectively. The shift of absorption intensity towards higher wavelength is observed well in the absorption spectra as discussed in earlier (see Fig. 4a). It depicts the onset of absorption in the visible region from wavelength of nearly 350 nm which is similar to the visible light photocatalyst CdS–ZnS/ZTP, as reported by Biswal et al.[29,37] When the samples are excited at this particular wavelength, an intense emission peak appears at ~700 nm wavelength for all the samples. Unlike absorption spectra, the PL emission spectra do not shift to higher wavelength but shows change in intensity with respect to WO$_3$ loading. The change in intensity follows the sequence of 10% WO$_3$ < ZnO < 50% WO$_3$ < 70% WO$_3$ < WO$_3$, respectively.
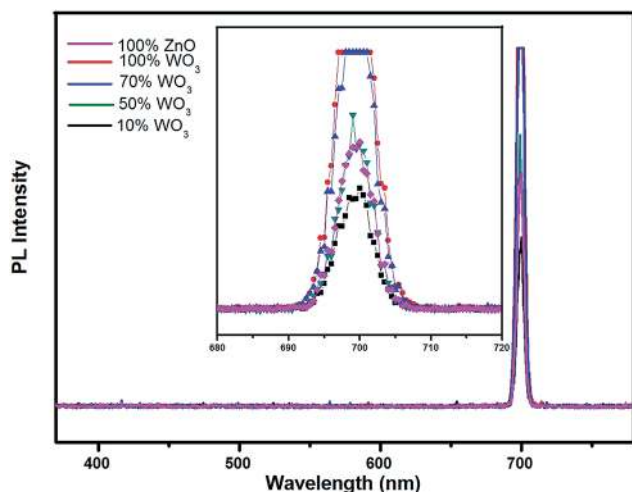

Fig. 11 Composite photoluminescence spectra of WO$_3$, ZnO and WO$_3$–ZnO mixed oxide composites with different WO$_3$ loading.

The PL intensity is suppressed in the presence of 10% WO$_3$ with ZnO. Pure WO$_3$ shows the maximum intensity that depicts the highest recombination rate. The reduction in intensity directly relates to the suppression of the electron–hole recombination rate. The reduced recombination rate reveals the efficient charge transfer within the catalyst mixture.[38] This means that more hydroxyl radicals $^\cdot OH$ can be produced in the system containing 10% WO$_3$–ZnO than that containing pure WO$_3$, which is advantageous to the visible light photocatalytic activity of WO$_3$. Increasing WO$_3$ content may lead to low electron accepting efficiency of ZnO due to less amount of ZnO in nanocomposites. This can prove as a disadvantage to the visible light photocatalytic activity of the composites. Consequently, the visible light photocatalytic activity of the investigated composites increases at first and then decreases as the WO$_3$ content increases.

4. Conclusions

An optimum amount 1 : 9 of nanocuboid WO$_3$ and quasi fiber ZnO was found to be an effective mixed oxide mixture for the photocatalytic decomposition of methylene blue and orange G, respectively. WO$_3$ acts as absorber of solar energy and ZnO as co-catalyst to reduce the electron–hole recombination. However, higher content of WO$_3$ beyond 10 wt% decreases the photocatalytic activity due to increasing recombination rate of electron–hole pairs, as supported by the increasing intensity in photoluminescence spectra. The recombination rate is found to reduce in the presence of 10 wt% WO$_3$. The mixed oxide can be reused effectively though the degree of efficiency slightly decreases with increasing number of cycles.

Acknowledgements

References

1 Y. Zheng, C. Chen, Y. Zhan, X. Lin, Q. Zheng, K. Wei and J. Zhu, *J. Phys. Chem. C*, 2008, **112**, 10773–10777.

2 P. A. Deshpande, S. Polisetti and G. Madras, *Langmuir*, 2011, **27**, 3578–3587.

3 G. Ciardelli, L. Corsi and M. Marcucci, *Resour., Conserv. Recycl.*, 2001, **32**, 189–197.

4 W. J. Lau and A. F. Ismail, *Desalination*, 2009, **245**, 321–348.

5 Y. Khambhaty, K. Mody, S. Basha and B. Jha, *Chem. Eng. J.*, 2009, **145**, 489–495.

6 C. A. Martinez-Huitle and E. Brillas, *Appl. Catal., B*, 2009, **87**, 105–145.

7 I. Oller, S. Malato and J. A. Sanchez-Perez, *Sci. Total Environ.*, 2011, **409**, 4141–4166.

8 S. A. Singh and G. Madras, *Sep. Purif. Technol.*, 2013, **105**, 79–89.

9 S. Yang, H. Yang, H. Ma, S. Guo, F. Cao, J. Gong and Y. Deng, *Chem. Commun.*, 2011, **47**, 2619–2621.

10 S. Yang, X. Cui, J. Gong and Y. Deng, *Chem. Commun.*, 2013, **49**, 4676–4678.

11 N. Huo, Q. Yue, J. Yang, S. Yang and J. Li, *ChemPhysChem*, 2013, **14**, 4069–4073.

12 A. Fujishima and K. Honda, *Nature*, 1972, **238**, 37–38.

13 R. Qiu, D. Zhang, Y. Mo, L. Song, E. Brewer, X. Huang and Y. Xiong, *J. Hazard. Mater.*, 2008, **156**, 80–85.

14 R. C. Pawar, V. Khare and C. S. Lee, *Dalton Trans.*, 2014, **43**, 12514–12527.

15 R. Y. Hong, J. H. Li, L. L. Chen, D. Q. Liu, H. Z. Li, Y. Zheng and J. Ding, *Powder Technol.*, 2009, **189**, 426–432.

16 L. Zheng, Y. Zheng, C. Chen, Y. Zhan, X. Lin, Q. Zheng, K. Wei and J. Zhu, *Inorg. Chem.*, 2009, **48**, 1819–1825.

17 S. Adhikari and D. Sarkar, *RSC Adv.*, 2014, **4**, 20145–20153.

18 S. Adhikari and D. Sarkar, *Electrochim. Acta*, 2014, **138**, 115–123.

19 J. Lin, J. Lin and Y. Zhu, *Inorg. Chem.*, 2007, **46**, 8372–8378.

20 D. S. Martinez, A. M. Cruz and E. L. Cuellar, *Appl. Catal., A*, 2011, **398**, 179–186.

21 M. Aslam, I. M. I. Ismail, S. Chandrasekaran and A. Hameed, *J. Hazard. Mater.*, 2014, **276**, 120–128.

22 L. Zhang, L. Yin, C. Wang, N. Lun and Y. Qi, *ACS Appl. Mater. Interfaces*, 2010, **2**, 1769–1773.

23 P. R. Potti and V. C. Srivastava, *Ind. Eng. Chem. Res.*, 2012, **51**, 7948–7956.

24 S. Lam, J. Sin, A. Z. Abdullah and A. R. Mohamed, *Ceram. Int.*, 2013, **39**, 2343–2352.

25 C. Yu, K. Yang, Q. Shu, J. C. Yu, F. Cao and X. Li, *Chin. J. Catal.*, 2011, **32**, 555–565.

26 J. Xei, Z. Zhou, Y. Lian, Y. Hao, X. Liu, M. Li and Y. Wei, *Ceram. Int.*, 2014, **40**, 12519–12524.

27 S. Adhikari, D. Sarkar and G. Madras, *RSC Adv.*, 2014, **4**, 55807–55814.

28 A. Sutka and G. Mezinskis, *Front. Mater. Sci.*, 2012, **6**, 128–141.

29 N. Biswal, D. P. Das, S. Martha and K. M. Parida, *Int. J. Hydrogen Energy*, 2011, **36**, 13452–13460.

30 Y. J. Li, X. D. Li, J. W. Li and J. Yin, *Water Res.*, 2006, **40**, 1119–1126.

31 J. Matos, J. Laine and J. M. Hermann, *Appl. Catal., B*, 1998, **18**, 281–291.

32 B. Subash, B. Krishnakumar, M. Swaminathan and M. Shanthi, *Langmuir*, 2013, **29**, 939–949.

33 Y. Yang, T. Zhang, L. Le, X. Ruan, P. Fang, C. Pan, R. Xiong, J. Shi and J. Wei, *Sci. Rep.*, 2014, DOI: 10.1038/srep07045.

34 R. Yin, Q. Luo, D. Wang, H. Sun, Y. Li, X. Li and J. An, *J. Mater. Sci.*, 2014, **49**, 6067–6073.

35 M. T. Uddin, Y. Nicolas, C. Olivier, T. Toupance, L. Servant and M. M. Muller, *Inorg. Chem.*, 2012, **51**, 7764–7773.

36 Y. J. Wang, R. Shin, J. Lin and Y. F. Zhu, *Energy Environ. Sci.*, 2011, **113**, 4605–4611.

37 S. Yang, Q. Yue, F. Wu, N. Huo, Z. Chen, J. Yang and J. Li, *J. Alloys Compd.*, 2014, **597**, 91–94.

38 X. Bai, L. Wang and Y. Zhu, *ACS Catal.*, 2012, **2**, 2769–2778.